RESEARCH ARTICLE
ATMOSPHERIC PHYSICS

Earth and Planetary Physics
6: 219–227, 2022
doi: 10.26464/epp2022029

Joint observation of the concentric gravity wave event on the Tibetan Plateau

Chang Lai[1,2*], PengWei Li[1], JiYao Xu[2], Wei Yuan[2], Jia Yue[3], Xiao Liu[4], Kogure Masaru[5], and LiLi Qian[1]

[1]School of Science, Chongqing University of Posts and Telecommunications, Chongqing 400065, China;

[2]State Key Laboratory of Space Weather, Center for Space Science and Applied Research, Chinese Academy of Sciences, Beijing 110000, China;

[3]Department of Physics, Catholic University of America, Washington, DC 20064, USA;

[4]College of Mathematics and Information Science, Henan Normal University, Xinxiang 410700, China;

[5]Department of Earth and Planetary Science, Kyushu University, Fukuoka 8190395, Japan

Key Points:

- A concentric gravity wave event over the Tibetan Plateau is reported based on joint observations from ground photographs, satellite imaging, and an all-sky airglow imager.
- The propagation trajectory of the wave packet was deduced by the ray-tracing method, and the wave source was identified as deep convection in Bangladesh.
- The propagation characteristics of the gravity waves were analyzed by wind filtering and wave ducting.

Citation: Lai, C., Li, P. W., Xu, J. Y., Yuan, W., Yue, J., Liu, X., Masaru, K., and Qian, L. L. (2022). Joint observation of the concentric gravity wave event on the Tibetan Plateau. *Earth Planet. Phys.*, *6*(3), 219–227. http://doi.org/10.26464/epp2022029

Abstract: A concentric gravity wave event was captured by a photographer in Nagarzê County (90.28°N, 28.33°E) between 02:00 and 04:00 (local time) on May 11, 2019. This concentric gravity wave event was also observed by the Suomi National Polar-orbiting Partnership satellite and the all-sky airglow imager at Yangbajing station (90.5°E, 30.1°N). The temporal and spatial information on gravity waves from the photographs provided a rare opportunity to study the propagation of gravity waves over the Tibetan Plateau. According to wind and temperature data from the MERRA-2 reanalysis (Modern-Era Retrospective analysis for Research and Applications, Version 2) and empirical models (NRLMSISE-00 [Naval Research Laboratory Mass Spectrometer and Incoherent Scatter Radar Exosphere] and HWM [horizontal wind model]), we inversely derived the propagation trajectory from the observed wave pattern to the source region by using the ray-tracing method. The source of the concentric gravity wave was identified as deep convection in Bangladesh (90.6°E, 25.0°N). The maximum background wind speed in the propagation direction (31.05 m/s) was less than the phase speed of 53 m/s, which is consistent with the wind-filtering theory.

Keywords: concentric gravity wave; ray-tracing method; convection source; Tibetan Plateau

1. Introduction

When the atmosphere is displaced from its equilibrium position, it produces disturbances resulting from the combined effects of gravity and buoyancy. This disturbance propagates into the upper atmosphere and is well known as an atmospheric gravity wave (GW; Holton, 1992). Gravity waves are an important means of transferring energy and momentum from the troposphere to the stratosphere, mesosphere, and thermosphere (McFarlane, 1987). Through momentum and energy transfer and deposition, GWs influence the atmosphere between the stratosphere and the entire thermosphere (Hodges, 1967; Lindzen, 1981). Gravity waves generated by flow over orography may break up in the stratosphere, causing clear air turbulence and threatening aviation safety (Regmi et al., 2017). Those with small amplitudes and long wavelengths can propagate upward to the thermosphere and ionosphere, affecting telecommunication (Azeem et al., 2015) in and the composition of the thermosphere (Qian et al., 2013). Gravity waves triggered by thunderstorms (Dewan et al., 1998), typhoons (Suzuki et al., 2013a), and tropical cyclones (Yue et al., 2014) may have a concentric pattern; thus, they are also called concentric GWs (CGWs). The secondary wave can be a CGW as well (Kogure et al., 2020). The generation and propagation characteristics of CGWs are closely related to their local convective environment (Fritts and Alexander, 2003).

When GWs reach a height of 87 ± 5 km (i.e., the OH airglow layer), the airglow of the OH will be disturbed and exhibit wave patterns. An all-sky airglow imager (ASAI) can detect the 715–930 nm band and track GWs in the OH airglow layer (Xu et al., 2015). Suzuki et al. (2007) reported a CGW event captured in both the OH and OI airglow layers (96 km), based on ASAI observations, and identified

Correspondence to: C. Lai, laichang@cqupt.edu.cn
Received 05 MAR 2022; Accepted 06 APR 2022.
Accepted article online 25 APR 2022.

the wave source as a cumulonimbus. They concluded that the weak wind system was the reason the waves were able to reach the upper atmosphere (Suzuki et al., 2007). Yue et al. (2009) studied nine CGW events spotted over Fort Collins, Colorado, from 2003 to 2008 and suggested that a weak background horizontal wind is a necessary condition for the observation of whole circular wave patterns in the OH layer. Model studies also support this conclusion (Vadas et al., 2009).

In addition to the ASAI, satellites provide a nadir view of GWs with a wide horizontal coverage and high spatial resolution. Because sun-synchronous polar satellites cannot offer temporal information, studies on CGW events often combine data from ASAIs and satellites. From joint observations of the Aqua satellite (Aumann et al., 2003), the Suomi National Polar-orbiting Partnership (Suomi NPP) satellite (Miller et al., 2015), and the ASAI network in the North China Plain, Xu et al. (2015) reported two CGW events triggered by thunderstorms in 2015 and discussed the free propagation and duct propagation of GWs.

To study the propagation characteristics of GWs, Jones (1969) proposed the ray-tracing method, which was further developed by Eckermann et al. (1992) and Vadas and Fritts (2009) to trace the propagation of GWs. The ray-tracing method tracks the trajectory of the observed GW packet to the region where the GW is generated based on the background wind speed, temperature, and parameters of the GWs. Using backward ray-tracing technology, Wrasse et al. (2006) derived the sources of GW events observed by the Cacheira Paulista Observatory in Brazil and the Tanjungsari Observatory in Indonesia and pointed out the difference in the wave source distribution of GWs at different geographic locations.

Concentric GWs excited by thunderstorms in Bangladesh were observed over the Tibetan Plateau (Chou et al., 2016). However, the propagation of GWs over the Tibetan Plateau has not been analyzed in detail because there are no ground observation stations in southern Tibet, and satellite observations lack temporal information. A group of CGW photographs taken by a photographer on May 11, 2019, provided a unique opportunity to study the propagation of CGWs over the Tibetan Plateau. From the combination of photographs, satellite observations, and the ASAI, this study revealed the nature of the source and propagation of the CGW event. In Section 2, we illustrate the CGW wave patterns captured by the camera of the photographer, the Suomi NPP satellite, and the ASAI. In Section 3, we locate the wave source by the ray-tracing method and identify it as deep convection in Bangladesh, which was supported by the cold brightness temperature. We then explain the propagation of the CGW based on satellite and ASAI observations. Finally, we discuss our findings and present our conclusions in Section 4.

2. Observations

2.1 Ground-based Camera

Photographs of the CGW event were captured by the photographer Lili Qian near Nagarzê County, Tibet Province, China (90.28°N, 28.33°E), between 02:00 and 04:00 (local time [LT]) on May 11, 2019 (18:00–20:00 universal time [UT] on May 10, 2019), with a Sony A7R3 camera. The camera was equipped with a Teng Long E 28–75 mm F/2.8 SLR lens with an exposure time of 20 s. The period of CGWs was the time interval of two adjacent wave surfaces arriving at the same point in the photographs. We measured the time interval of four wave surfaces in a row (Figures 1a–1d) and obtained the period (12.5 ± 0.3 min) by the averaging method.

To confirm the elevation and azimuth (clockwise from the north), 40 stars in the background were chosen for comparison with those given by Stellarium (Figure 2a). Stellarium is a software that shows a realistic starry sky watched at a given time and position with elevation–azimuth coordinates. The elevation and azimuth in the photographs could be obtained by comparing the corresponding bright stars in the photographs and Stellarium. Twelve anchor points were evenly distributed along the three most clearly visible wave surfaces, with four points for each wave surface (Figure 2b). The wave surfaces were then projected onto the geographic coordinates according to the horizontal distances between the wave surface and the ground-based camera and azimuths of the anchor points (Figure 2c). From Figure 2c, the horizontal wavelength could be measured as 40 km. The azimuth φ, elevation θ, and horizontal distance x from each anchor point to the camera for the 12 points are listed in Table 1.

2.2 Suomi NPP Satellite

As the photographer captured the photographs, the Suomi NPP satellite skimmed over the Tibetan Plateau and recorded the CGW structures at 03:46 LT on May 11, 2019. The day/night band (DNB) of the Visible/Infrared Imaging Radiometer Suit (VIIRS) onboard the satellite was focused on wavelengths between 500 and 900 nm, which enabled the Suomi NPP satellite to capture the disturbances in the OH layer with a horizontal resolution of 0.74 km. The satellite is on a sun-synchronous polar orbit, scanning a swath 3, 000 km in width (Miller et al., 2012). The wave patterns propagating to the northeast had a horizontal wavelength of 41 km, which was similar to that of the CGWs captured by the photographer (Figure 3).

2.3 All-Sky Airglow Imager

To the north of the photographer, the ASAI deployed at Yangbajing station (90.5°E, 30.1°N) recorded this CGW event as well. The ASAI consists of an optical imaging system sensitive to the OH emission band, a control system, and a charged-coupled device (CCD) with 1,024 × 1,024 pixels for storage. The ASAI takes pictures of the night sky at an effective zenith angle of 160°, one picture every 64 s (Xu et al., 2015). Owing to cloud obstacles, the CGW event was observed by the ASAI from only 04:00 to 04:30 (Figure 4), moving northward with a wavelength of 40 km for a period of 8 ± 1 min.

2.4 Images Assembled from the Three Instruments

For comparison, the wave patterns observed by the camera, satellite, and ASAI are shown in Figure 5 based on their geographic coordinates. The propagation parameters of the CGWs measured by the three observers are listed in Table 2. On the basis of their structure, location, and time, the two wave patterns captured by the camera and satellite appeared to have been triggered by one source, although satellite images cannot provide temporal information. The differences in period and phase speed derived

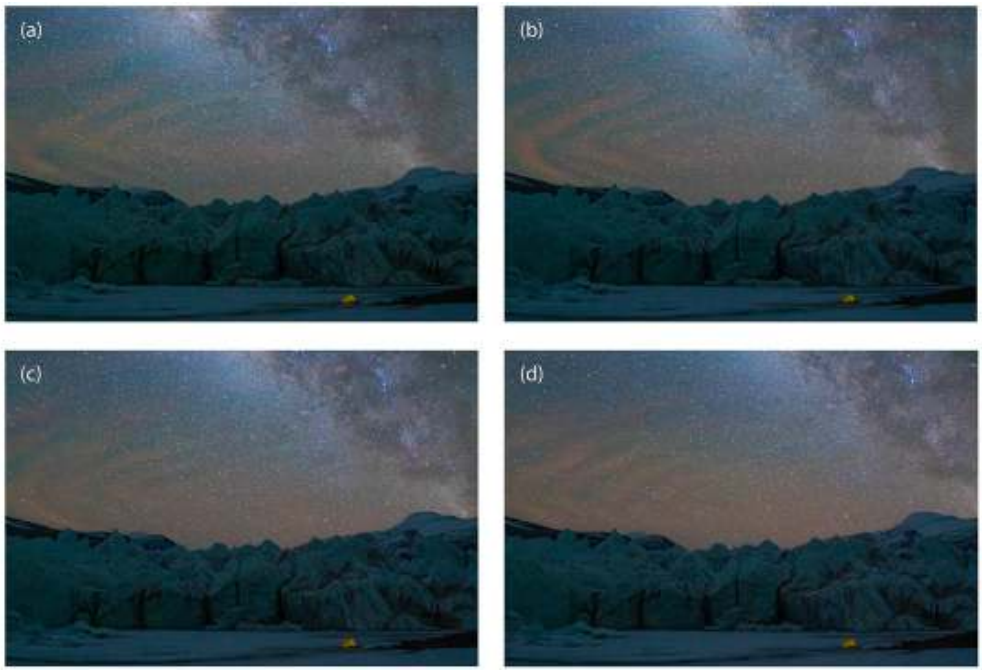

Figure 1. Concentric gravity waves captured by the camera of a citizen scientist on the morning of May 11, 2019. Images (a), (b), (c), and (d) were captured at 03:09, 03:22, 03:35, and 03:48 LT, respectively. The wave patterns are orange, which may have been caused by the radiation of Na (589.3 nm) and OI (630 nm; Chou et al., 2016).

from the camera and ASAI may have been caused by their local wind fields.

3. Wave Source and Propagation

3.1 Ray-Tracing Method

The ray-tracing method was applied to derive the source of the CGWs. To backward-trace the propagation path of the wave, the velocities of the wave packets were calculated every 100 m in height according to parameters such as the wind field, temperature, wavenumber, and frequency. The zonal, meridional, and vertical components of the group velocities, C_{gx}, C_{gy}, and C_{gz}, could be derived as follows:

$$C_{gx} = \frac{\mathrm{d}x}{\mathrm{d}t} = \frac{k_x\left(N^2 - \hat{\omega}^2\right)}{\hat{\omega}\Delta} + U, \tag{1}$$

$$C_{gy} = \frac{\mathrm{d}y}{\mathrm{d}t} = \frac{k_y\left(N^2 - \hat{\omega}^2\right)}{\hat{\omega}\Delta} + V, \tag{2}$$

$$C_{gz} = \frac{\mathrm{d}z}{\mathrm{d}t} = -\frac{m\hat{\omega}^2}{\hat{\omega}\Delta}, \tag{3}$$

where k_x and k_y denote the zonal and meridional wavenumbers, respectively, $\hat{\omega}$ is the intrinsic frequency,

$$\hat{\omega} = \omega - k_x U - k_y V, \tag{4}$$

and ω is the apparent frequency. Variables U and V are the zonal and meridional wind speeds, respectively. The Δ in Equation (1) can be expressed as

$$\Delta = k_x^2 + k_y^2 + m^2 + \frac{1}{4h^2}, \tag{5}$$

where h indicates the density scale height, which was taken as 7 km in our calculation. According to the dispersion relation, the vertical wavenumber m of the wave packet can be written as

$$m^2 = \frac{N^2}{(C-u)^2} + \frac{u_{zz}}{(C-u)} - (k_x^2 + k_y^2), \tag{6}$$

where u is the component of wind speed in the propagation direction of the waves, u_{zz} is the second derivative of u over height z, and C is the intrinsic phase speed of the wave packets. The N is controlled by the background thermal structure, and it influences the generation, propagation, and dissipation of GWs (Liu et al., 2020):

$$N = \sqrt{\frac{g}{T}\left(\frac{\mathrm{d}T}{\mathrm{d}z} + \Gamma_d\right)}, \tag{7}$$

where T is the atmospheric temperature, g is the gravitational acceleration, and Γ_d (Nappo, 2002) is the adiabatic decline rate. In Equations (3) and (6), the Coriolis frequency is neglected because it is very small compared with the frequency of the CGW.

The intrinsic frequency $\hat{\omega}$ and squared vertical wavenumber m^2 were calculated based on Equations (4) and (6) at every 100 m in height to deduce the corresponding C_{gz}. According to the velocities calculated by using Equations (1) to (3), the propagation of wave packets was traced backward with a C_{gz}-dependent temporal step of 100 m/C_{gz}. The cutoff conditions in the ray-tracing model included (1) $m^2 \leq 0$, a turning lever, that is, the GWs become reflected; (2) $m^2 > 1 \times 10^{-6}$ (cyc^2· m^{-2}) (Wrass et al., 2006); under this condition, the GW almost reaches the critical layer, and its vertical wavelength is less than 1 km; and (3) $|m| \to \infty$, where the GW packet is breaking. The tracing process stops when any of the cutoff conditions is triggered, and this position is regarded as a possible source of the observed GW.

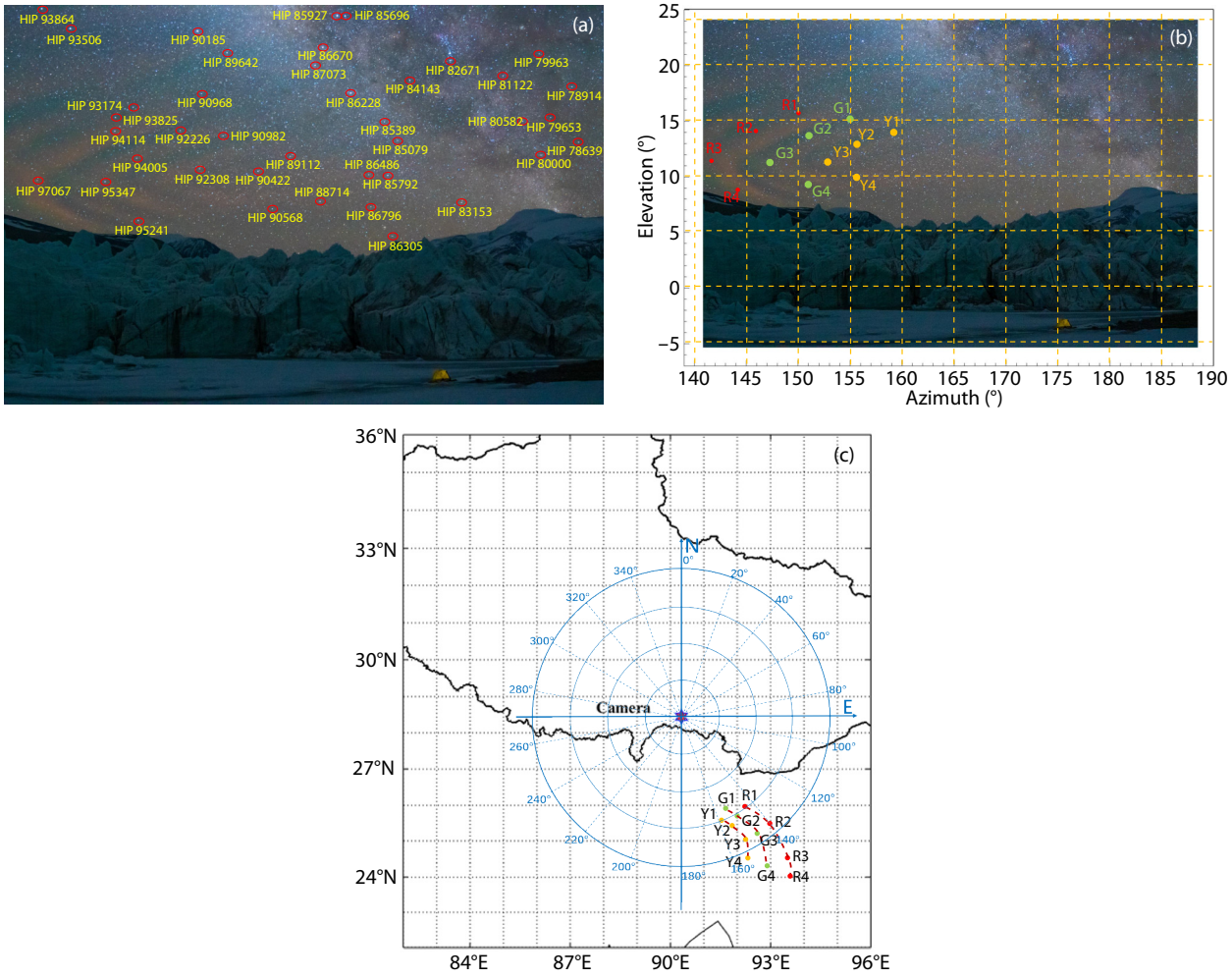

Figure 2. Projection of gravity waves in the photographs onto geographic coordinates. (a) Markers of the 40 stars. HIP indicates the HIPPARCOS catalogue (Perryman et al., 1997). (b) Selected anchor points for projection. R, G, and Y indicate the red, green and yellow points, respectively. (c) Wave fronts projected onto the geographic coordinates. In the polar coordinates, the original position is the photographing position and the angle is the azimuth.

Table 1. Location parameters of the anchor points.[a]

Point	R1	R2	R3	R4	G1	G2	G3	G4	Y1	Y2	Y3	Y4
φ (°)	150	140	141	144	155	151	147	151	159	156	153	156
θ (°)	15.7	14.1	11.3	8.8	15.1	13.6	11.3	9.2	14.0	12.9	11.3	9.9
x (km)	310	346	435	562	322	360	435	537	349	380	435	498

[a]The azimuth is clockwise from the north. The equation $x = H/\tan\theta$ is the horizontal distance from each point to the camera, where H is the height of the OH layer (87 km). R, G, and Y indicate the red, green and yellow points in Figure 2b, respectively.

3.2 Wave Source

The CGWs photographed over the Tibetan Plateau were ray-traced and analyzed based on model wind conditions. Wind profiles from the Modern-Era Retrospective analysis for Research and Applications, Version 2 (MERRA-2, 0–77 km; Rienecker et al., 2011) and horizontal wind model (HWM, 80–87 km; Hedin et al., 1996) were used. Temperature profiles were obtained from the MERRA-2 and the Naval Research Laboratory Mass Spectrometer and Incoherent Scatter Radar Exosphere (NRLMSISE-00, 80–87 km; Picone et al., 2002). A temperature and wind speed between 77 and 80 km were the average from MERRA-2 and the empirical models (HWM and NRLMSISE-00). Because of the lack of observation data, we had to use the empirical models to derive temperatures and wind speeds greater than 77 km. The distributions of the temperature and zonal and meridional wind speeds along the height are shown in Figure 6. Horizontal variation in the wind and temperature were neglected.

On the basis of the background parameters in Figure 6 and the wave parameters taken by the camera presented in Table 2, we could obtain the initial wavenumbers: the zonal, meridional, and

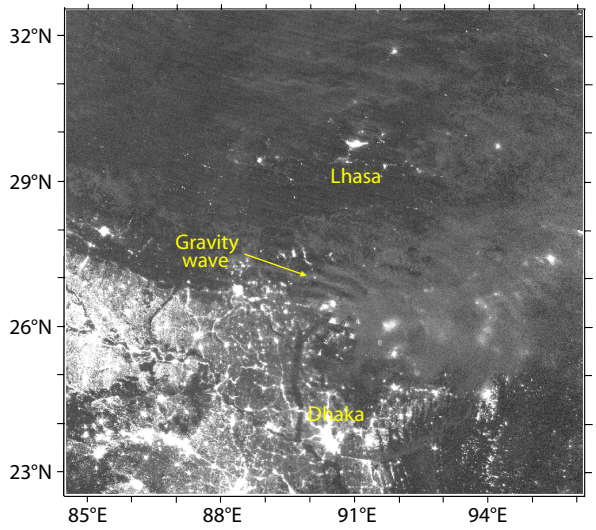

Figure 3. The concentric gravity wave (CGW) patterns observed over the Tibetan Plateau by VIIRS/DNB at 03:46 LT on May 11, 2019. The CGW had a horizontal wavelength of 41 km and propagated to the northeast.

vertical wavenumbers were 9.0×10^{-5} rad/m, 1.2×10^{-4} rad/m, and 2.6×10^{-4} rad/m, respectively. The intrinsic frequency $\hat{\omega}$, buoyancy frequency N, and Squared vertical wave number m^2 at different heights were derived by the ray-tracing model (Figures 7a–7d). The square of the vertical wavenumber approached zero at an altitude of 8.0 km, so ray tracing was terminated in the troposphere. From the propagation parameters, the latitudinal and meridional propagation trajectories of the wave were obtained, and the source of the CGW was located at 25.0°N, 90.6°E.

A brightness temperature map (Figure 8a) provided by the Suomi NPP satellite showed that the temperature changed significantly near the wave source and that deep convection could have acted as the source of the CGW event. The convective precipitation from the ERA5 (ECMWF Reanalysis 5th Generation) data (Hersbach and Dee, 2016) at 4:00 LT on May 11, 2019 (Figure 8b), indicated that rainfall was caused by convection in the source area, which further indicated that the CGW was triggered by deep convection.

3.3 Wave Propagation

Owing to the strong horizontal wind in the area near the wave source, the wave patterns of the CGWs were captured only from north to east of the source. The maximum zonal wind speed below a height of 87 km was 48 m/s (Figure 9b), which exceeded the weak wind speed of 20 m/s required to observe the complete concentric waveforms (Suzuki et al., 2007; Yue et al., 2009). In the azimuth range of 0°–30° from the wave source, arc-shaped wave forms were captured by the Suomi NPP satellite (Figure 9a), whereas no wave patterns were visible in the opposite direction. The strong background wind may be one of the reasons why only a part of the complete circular wave fronts was observed. According to the wind-filtering theory, the wave speed observed should be greater than the wind speed in that direction; otherwise, the wave would be filtered out. The horizontal wind speeds along each direction were calculated by

$$u = V\cos\alpha + U\sin\alpha \tag{8}$$

and are shown in Figures 9c and 9d. Azimuth α is the azimuth from the north (Figure 9a). Wind speeds U and V are the meridional and zonal wind speeds, respectively (Figure 9b). By taking the northeast direction of propagation as positive, the horizontal wind speed reached a maximum of 31.05 m/s at a height of 11.4 km (Figure 9c) and a minimum of −44.15 m/s at a height of 64.5 km (Figure 9d). By taking the period obtained from the photographs as a reference, the speed of the wave patterns in Figure 9a could be estimated as 53 m/s, which is consistent with the requirement of the wind-filtering theory (Shi et al., 2021) that the ground-based phase speed of the CGW should be greater than the maximum wind speed in the northeast direction. The wave package could thus propagate upward and reach the OH layer. Southwest of the source, the phase speed of the CGW was greater than the wind speed in most directions, so the wave could propagate upward to the OH layer. However, a CGW was not spotted in the southwest, which may have been due to the bright ground urban light in India.

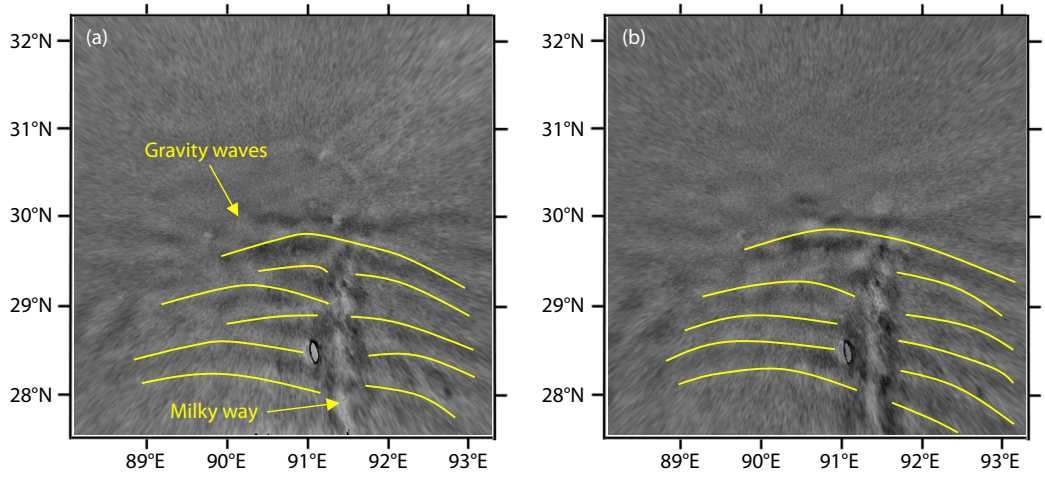

Figure 4. Concentric gravity wave patterns observed by the ASAI at 4:12 LT on May 11, 2019. The wave surfaces are highlighted with yellow curves.

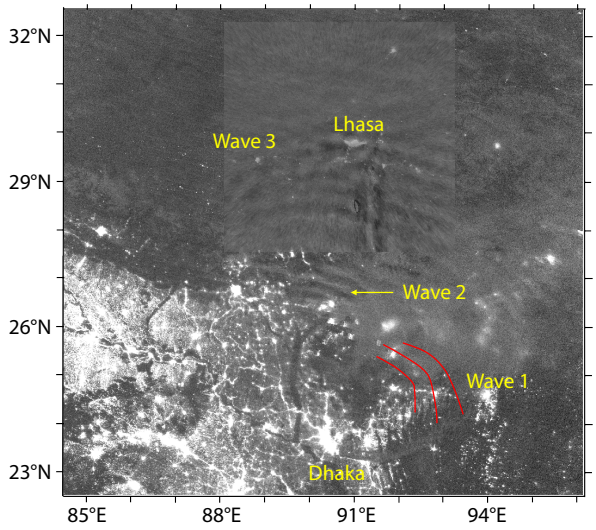

Figure 5. The combination of wave patterns. Wave 1, marked by the red curves, is the projection of wave patterns in the photograph. Waves 2 and 3 are concentric gravity waves captured by the satellite and ASAI, respectively.

The wave patterns captured by the ASAI were 400 km north of the wave source. The square of the vertical wavenumber m^2 of the wave patterns was derived based on temperature data from the NRLMSISE-00 model and wind field data from the HWM model (Figure 10). The m^2 approached zero at altitudes of 83 km and 120 km, where GWs were evanescent. The m^2 was positive within an altitude range of 83–120 km, so the GWs were ducted in this region. This could explain why the wavelength at 400 km north of the wave source was equal to that at 200 km, as spotted by the satellite (Suzuki et al., 2013b; Xu et al., 2015). In deriving m^2, the dispersion relation included the wind variation (Equation (6)). The change in temperature was also considered in calculating N in Equation (6) (see Equation (7)). Hence, the guided propagation was a combination of Doppler and thermal waveguides (Fritts and Yuan, 1989). Empirical models such as the HWM or NRLMSISE are not very accurate in the stratosphere and mesosphere. However, no other observations around provided the wind or temperature, so the propagation characteristics were analyzed based on the temperature and wind from empirical models greater than 80 km.

4. Conclusions

From 1:00 a.m. to 4:00 a.m. (LT) on May 11, 2019, the propagation of a CGW on the Tibetan Plateau was successively observed by a photographer, the Suomi NPP satellite, and the ASAI. From the horizontal wavelength, speed, and period extracted from the photographic sequence offered by the photographer,

Table 2. Comparison of wave parameters.[a]

Parameter	Camera	Satellite	ASAI
Time (UTC)	2019-5-11 03:22	2019-5-11 03:46	2019-5-11 04:12
Horizontal wavelength (km)	40 ± 1	40 ± 1	41 ± 1
Period (min)	12.5 ± 0.3	N/A	8 ± 1
Phase speed (m/s)	53 ± 2	N/A	85 ± 12

[a]The Suomi NPP satellite cannot track waves; therefore, the temporal information is absent. The uncertainty of the wavelength in the photographs arises from the variance among multiple measurements. The uncertainties of the wavelengths from the satellite and ASAI were decided by their resolution. The uncertainties of the period depended on the exposure time of the observation instruments. UTC, coordinated universal time.

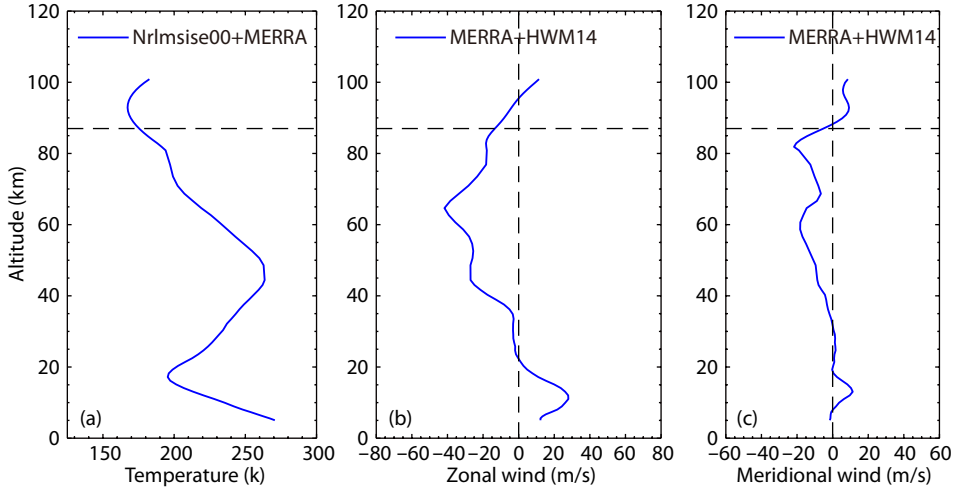

Figure 6. Profiles of the (a) temperature from MERRA-2 (0–77 km) and NRLESISE-00, (b) zonal wind, and (c) meridional wind from MERRA-2 (0–77 km) and the HWM at 02:00–04:00 LT on May 11, 2019. At a height of 87 km, the temperature is 176 K. The zonal and meridional wind speeds are −12 m/s and −1 m/s, respectively.

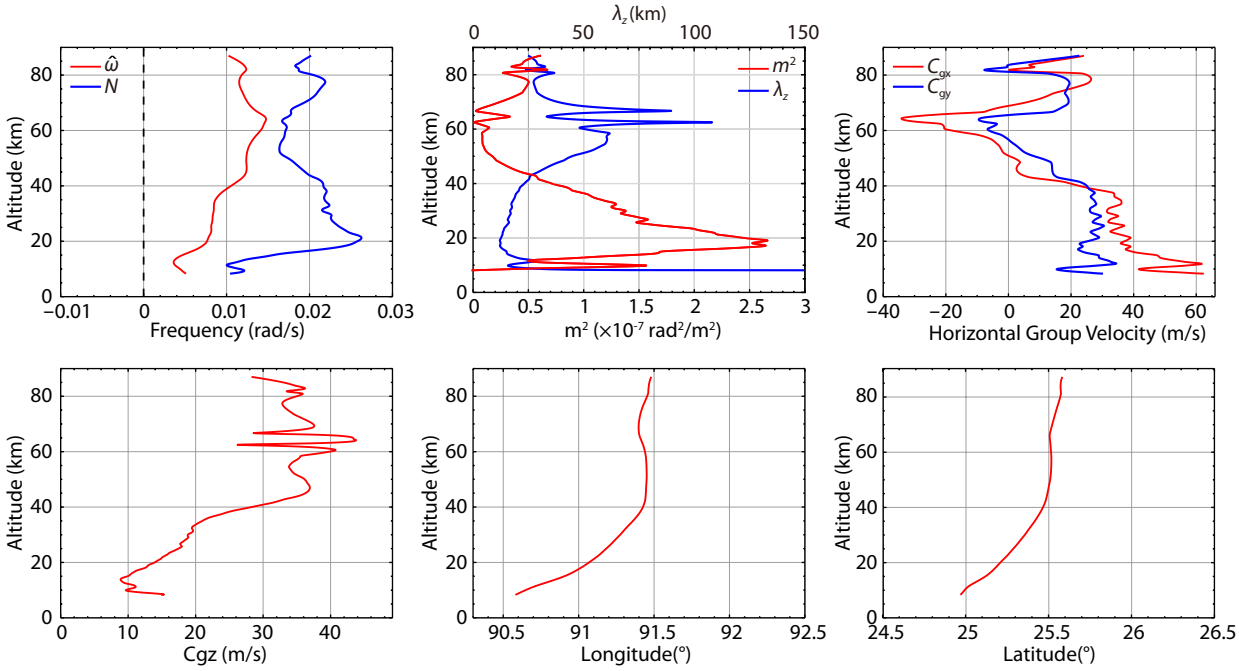

Figure 7. Backward ray-tracing results of the concentric gravity wave. (a) Intrinsic frequency $\hat{\omega}$ (red line) and buoyancy frequency N (blue line). (b) Squared vertical wavenumber m^2 (red line) and vertical wavelength (blue line). The square of wavenumber m^2 approaches zero and λ_z tends to infinity at 8.0 km. (c) Zonal group velocity (red line) and meridional group velocity (blue line). (d) Vertical group velocity. (e) Ray path for longitude–altitude. (f) Ray path for latitude–altitude.

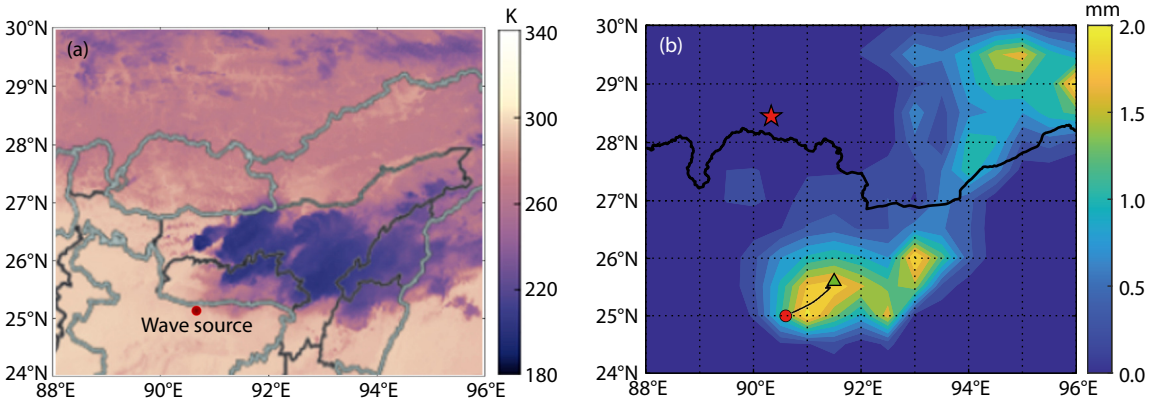

Figure 8. (a) Brightness temperature image at 03:50 LT on May 11, 2019. The red dot represents the wave source, and the color bar represents the brightness temperature. (b) Precipitation from ERA5 at 04:00 LT on May 11, 2019. The red star and the green triangle represent the position of the camera and the position of the wave packet in the photographs (91.5°E, 25.6°N). The black curve is the propagation path, and the red dot represents the wave source.

the source of the CGW was located at 25.0°N, 90.6°E. With the convective precipitation of ERA5 reanalysis data, the CGW was identified as having been triggered by a deep convection in Bangladesh.

In the joint field of view of the three observers, wave patterns were observed only from north to east. In the directions that wave patterns were observed, the horizontal wave speed was greater than the wind speed, which met the requirements of the wind-filtering theory. The waveforms recorded by the ASAI were 40 km north of the wave source. The variation in the square of the vertical wavenumber along the height indicated the presence of a conduction region between the heights of 83 and 120 km.

Photographers, satellites, and the ASAI rarely record the same CGW event. The photographs accidentally taken by the photographer provided temporal information that enabled us to identify the propagation characteristics of the CGW over the Tibetan Plateau. By combining the information in the photographs with the satellite and ASAI observations, we determined the wave source, analyzed the influence of the wind field on GW propagation, and found the ducting area. Owing to the limited coverage of scientific observations, high-quality airglow photographs taken

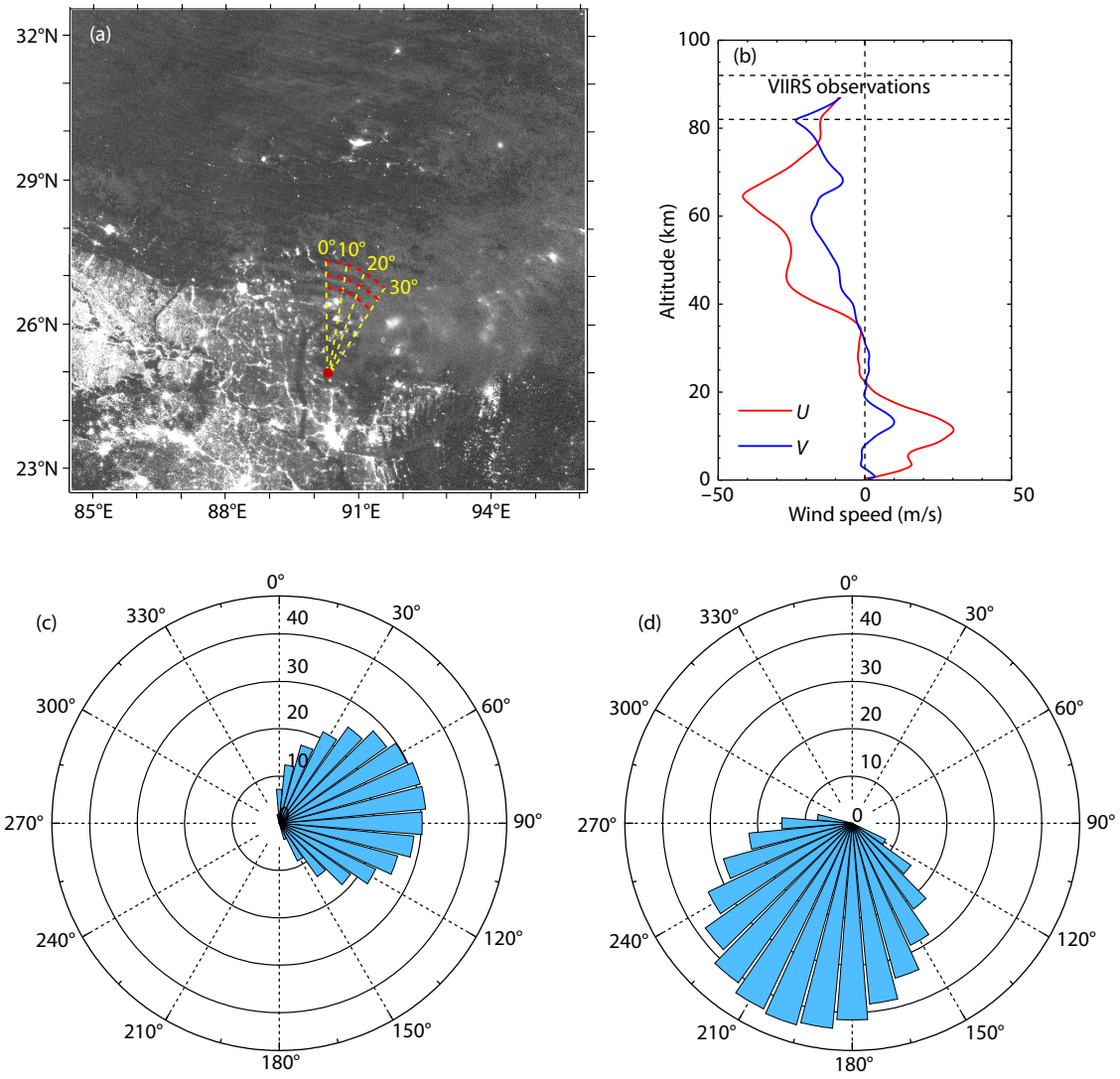

Figure 9. (a) The bending wave structure observed by the Suomi NPP satellite. The red arcs represent the wave surfaces. The wave source is denoted by the red point. The angle is the azimuth relative to the wave source. (b) The mean meridional and zonal wind speeds (24°–28°N, 88°–94°E). (c) Components of the horizontal wind speed at a height of 11.4 km. The wind speed reaches a maximum of 31.05 m/s at an azimuth of 80°. (d) Components of the horizontal wind speed at a height of 64.5 km. The wind speed reaches a maximum of 44.15 m/s at an azimuth of 200°.

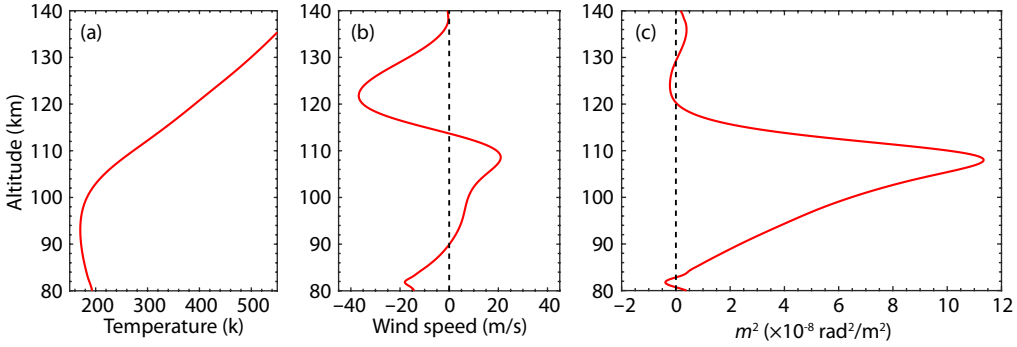

Figure 10. (a) Temperature, (b) wind speed, and (c) square of wavenumber m^2 of the concentric gravity wave captured by the ASAI. The temperature profile was provided by the NRLMSISE-00 model. The square of wavenumber m^2 reaches 0 at heights of 83 and 120 km.

by photographers are of great value for discovering the propagation characteristics of GWs on the Tibetan Plateau.

Acknowledgments

We thank Lili Qian for her photographs. This research was funded

by the Science Foundation of Chongqing (Grant No. cstc2020jcyj-msxmX0914), the Informatization Plan of the Chinese Academy of Sciences (Grant No. CAS-WX2021PY-0101), and the Specialized Research Fund for State Key Laboratories.

References

Aumann, H. H., Chahine, M. T., Gautier, C., Goldberg, M. D., Kalnay, E., McMillin, L. M., Revercomb, H., Rosenkranz, P. W., Smith, W. L., … Susskind, J. (2003). AIRS/AMSU/HSB on the Aqua mission: design, science objectives, data products, and processing systems. *IEEE Trans. Geosci. Remote Sens.*, *41*(2), 253–264. https://doi.org/10.1109/TGRS.2002.808356

Azeem, I., Yue, J., Hoffmann, L., Miller, S. D., Straka, W. C., III, and Crowley, G. (2015). Multisensor profiling of a concentric gravity wave event propagating from the troposphere to the ionosphere. *Geophys. Res. Lett.*, *42*(19), 7874–7880. https://doi.org/10.1002/2015GL065903

Chou, C. C., Dai, J., Kuo, C. L., and Huang, T. Y. (2016). Simultaneous observations of storm-generated sprite and gravity wave over Bangladesh. *J. Geophys. Res.: Space Phys.*, *121*(9), 9222–9233. https://doi.org/10.1002/2016JA022554

Dewan, E. M., Picard, R. H., O'Neil, R. R., Gardiner, H. A., Gibson, J., Mill, J. D., Richards, E., Kendra, M., and Gallery, W. O. (1998). MSX satellite observations of thunderstorm-generated gravity waves in mid-wave infrared images of the upper stratosphere. *Geophys. Res. Lett.*, *25*(7), 939–942. https://doi.org/10.1029/98GL00640

Eckermann, S. D. (1992). Ray-tracing simulation of the global propagation of inertia gravity waves through the zonally averaged middle atmosphere. *J. Geophys. Res.: Atmos.*, *97*(D14), 15849–15866. https://doi.org/10.1029/92jd01410

Fritts, D. C., and Yuan, L. (1989). An analysis of gravity wave ducting in the atmosphere: Eckart's resonances in thermal and Doppler ducts. *J. Geophys. Res.: Atmos.*, *94*(D15), 18455–18466. https://doi.org/10.1029/JD094iD15p18455

Fritts, D. C., and Alexander M. J. (2003). Gravity wave dynamics and effects in the middle atmosphere. *Rev. Geophys.*, *41*(1), 1003. https://doi.org/10.1029/2001RG000106

Hedin, A. E., Fleming, E. L., Manson, A. H., Schmidlin, F. J., Avery, S. K., Clark, R. R., Franke, S. J., Fraser, G. J., Tsuda, T., … Vincent, R. A. (1996). Empirical wind model for the upper, middle and lower atmosphere. *J. Atmos. Terr. Phys.*, *58*(13), 1421–1447. https://doi.org/10.1016/0021-9169(95)00122-0

Hersbach, H., and Dee, D. (2016). ERA5 reanalysis is in production. *ECMWF Newsletter*, 147.

Hodges, R. R. Jr. (1967). Generation of turbulence in the upper atmosphere by internal gravity waves. *J. Geophys. Res.*, *72*(13), 3455–3458. https://doi.org/10.1029/JZ072i013p03455

Holton, J. R. (1992). *An Introduction to Dynamic Meteorology* (3rd ed). San Diego: Academic Press.

Jones, W. L. (1969). Ray tracing for internal gravity waves. *J. Geophys. Res.*, *74*(8), 2028–2033. https://doi.org/10.1029/JB074i008p02028

Kogure, M., Yue, J., Nakamura, T., Hoffmann, L., Vadas, S. L., Tomikawa, Y., Ejiri, M. K., and Janches, D. (2020). First direct observational evidence for secondary gravity waves generated by mountain waves over the Andes. *Geophys. Res. Lett.*, *47*(17), e2020GL088845. https://doi.org/10.1029/2020GL088845

Lindzen, R. S. (1981). Turbulence and stress owing to gravity wave and tidal breakdown. *J. Geophys. Res.: Oceans*, *86*(C10), 9707–9714. https://doi.org/10.1029/JC086iC10p09707

Liu, X., Xu, J. Y., and Yue, J. (2020). Global static stability and its relation to gravity waves in the middle atmosphere. *Earth Planet. Phys.*, *4*(5), 504–512. https://doi.org/10.26464/epp2020047

McFarlane, N. A. (1987). The effect of orographically excited gravity wave drag on the general circulation of the lower stratosphere and troposphere. *J. Atmos. Sci.*, *44*(14), 1775–1800. https://doi.org/10.1175/1520-0469(1987)044<1775:TEOOEG>2.0.CO;2

Miller, S. D., Mills, S. P., Elvidge, C. D., Lindsey, D. T., Lee, T. F., and Hawkins, J. D. (2012). Suomi satellite brings to light a unique frontier of nighttime environmental sensing capabilities. *Proc. Natl. Acad. Sci. USA*, *109*(39), 15706–15711. https://doi.org/10.1073/pnas.1207034109

Miller, S. D., Straka, W. C., III, Yue, J., Smith, S. M., Alexander, M. J., Hoffmann, L., Setvák, M., and Partain, P. T. (2015). Upper atmospheric gravity wave details revealed in nightglow satellite imagery. *Proc. Natl. Acad. Sci. USA*, *112*(49), E6728–E6735. https://doi.org/10.1073/pnas.1508084112

Nappo, C. J. (2002). *An Introduction to Atmospheric Gravity Waves* (pp. 6–9). Amsterdam: Academic Press.

Perryman, M., Lindegren, L., Kovalevsky, J., et al. (1997). The HIPPARCOS catalogue. *Astron. Astrophys.*, 323, L49-L52.

Picone, J. M., Hedin, A. E., Drob, D. P., and Aikin, A. C. (2002). NRLMSISE-00 empirical model of the atmosphere: statistical comparisons and scientific issues. *J. Geophys. Res.: Space Phys.*, *107*(A12), 1468. https://doi.org/10.1029/2002ja009430

Qian, L. Y., Burns, A. G., Solomon, S. C., and Wang, W. B. (2013). Annual/semiannual variation of the ionosphere. *Geophys. Res. Lett.*, *40*(10), 1928–1933. https://doi.org/10.1002/grl.50448

Regmi, R. P., Kitada, T., Dudhia, J., and Maharjan, S. (2017). Large-scale gravity current over the middle hills of the Nepal Himalaya: implications for aircraft accidents. *J. Appl. Meteor. Climatol.*, *56*(2), 371–390. https://doi.org/10.1175/JAMC-D-16-0073.1

Rienecker, M. M., Suarez, M. J., Gelaro, R., Todling, R., Bacmeister, J., Liu, E., Bosilovich, M. G., Schubert, S. D., Takacs, L., … Woollen, J. (2011). MERRA: NASA's modern-era retrospective analysis for research and applications. *J. Climate*, *24*(14), 3624–3648. https://doi.org/10.1175/JCLI-D-11-00015.1

Shi, G. C., Hu, X., Yao, Z. G., Guo, W. J., Sun, M. C., and Gong, X. Y. (2021). Case study on stratospheric and mesospheric concentric gravity waves generated by deep convection. *Earth Planet. Phys.*, *5*(1), 79–89. https://doi.org/10.26464/epp2021002

Suzuki, S., Shiokawa, K., Otsuka, Y., Ogawa, T., Nakamura, K., and Nakamura, T. (2007). A concentric gravity wave structure in the mesospheric airglow images. *J. Geophys. Res.: Atmos.*, *112*(D2), D02102. https://doi.org/10.1029/2005JD006558

Suzuki, S., Vadas, S. L., Shiokawa, K., Otsuka, Y., Kawamura, S., and Murayama, Y. (2013a). Typhoon-induced concentric airglow structures in the mesopause region. *Geophys. Res. Lett.*, *40*(22), 5983–5987. https://doi.org/10.1002/2013GL058087

Suzuki, S., Shiokawa, K., Otsuka, Y., Kawamura, S., and Murayama, Y. (2013b). Evidence of gravity wave ducting in the mesopause region from airglow network observations. *Geophys. Res. Lett.*, *40*(3), 601–605. https://doi.org/10.1029/2012GL054605

Vadas, S. L., and Fritts, D. C. (2009). Reconstruction of the gravity wave field from convective plumes via ray tracing. *Ann. Geophys.*, *27*(1), 147–177. https://doi.org/10.5194/angeo-27-147-2009

Vadas, S. L., Yue, J., She, C. Y., Stamus, P. A., and Liu, A. Z. (2009). A model study of the effects of winds on concentric rings of gravity waves from a convective plume near Fort Collins on 11 May 2004. *J. Geophys. Res.: Atmos.*, *114*(D6), D06103. https://doi.org/10.1029/2008JD010753

Wrasse, C. M., Nakamura, T., Tsuda, T., Takahashi, H., Medeiros, A. F., Taylor, M. J., Gobbi, D., Salatun, A., Suratno, … Admiranto, A. G. (2006). Reverse ray tracing of the mesospheric gravity waves observed at 23°S (Brazil) and 7°S (Indonesia) in airglow imagers. *J. Atmos. Sol.-Terr. Phys.*, *68*(2), 163–181. https://doi.org/10.1016/j.jastp.2005.10.012

Xu, J. Y., Li, Q. Z., Yue, J., Hoffmann, L., Straka, W. C., III, Wang, C. M., Liu, M. H., Yuan, W., Han, S. … Ning, B. Q. (2015). Concentric gravity waves over northern China observed by an airglow imager network and satellites. *J. Geophys. Res.: Atmos.*, *120*(21), 11058–11078. https://doi.org/10.1002/2015JD023786

Yue, J., Vadas, S. L., She, C. Y., Nakamura, T., Reising, S. C., Liu, H. L., Stamus, P., Krueger, D. A., Lyons, W., and Li, T. (2009). Concentric gravity waves in the mesosphere generated by deep convective plumes in the lower atmosphere near Fort Collins, Colorado. *J. Geophys. Res.: Atmos.*, *114*(D6), D06104. https://doi.org/10.1029/2008JD011244

Yue, J., Miller, S. D., Hoffmann, L., and Straka, W. C., III. (2014). Stratospheric and mesospheric concentric gravity waves over tropical cyclone Mahasen: joint AIRS and VIIRS satellite observations. *J. Atmos. Sol.-Terr. Phys.*, *119*, 83–90. https://doi.org/10.1016/j.jastp.2014.07.003